On the role of aortic valve architecture for physiological haemodynamics and valve replacement. Part I: flow topology and vortex dynamics

Pascal Corso (pascal.corso@unibe.ch)
University of Bern https://orcid.org/0000-0001-7875-1080
Dominik Obrist
University of Bern

Research Article

Keywords: Aortic stenosis, Aortic valve replacement, Bioprosthetic aortic valve, Jet flow, Valve design, Vortical structures, Vorticity transport

Posted Date: September 27th, 2023

DOI: https://doi.org/10.21203/rs.3.rs-3385983/v1

On the role of aortic valve architecture for physiological haemodynamics and valve replacement. Part I: flow topology and vortex dynamics.

Pascal Corso[1], Dominik Obrist[1]

Affiliation: [1]ARTORG Center for Biomedical Engineering Research, University of Bern, Bern, Switzerland.

Correspondence: Pascal Corso, University of Bern, Bern, Switzerland.
E-mail: pascal.corso@unibe.ch

Abstract

Aortic valve replacement has become a growing concern due to the increasing prevalence of aortic stenosis in an ageing population. Existing replacement options have limitations, necessitating the development of improved prosthetic aortic valves. In this study, flow characteristics during systole in a stenotic aortic valve case are compared with those downstream of two newly designed surgical bioprosthetic aortic valves (BioAVs) using advanced simulations. Our findings reveal that the stenotic case maintains a high jet flow eccentricity due to a fixed orifice geometry, resulting in increased vortex stretching in the commissural low-flow regions. One BioAV design introduces non-axisymmetric leaflet motion, which reduces the maximum jet velocity and forms more vortical structures. The other BioAV design produces a fixed symmetric triangular jet shape due to non-moving leaflets and exhibits favourable vorticity attenuation and significantly reduced drag. Therefore, this study highlights the benefits of custom-designed aortic valves in the context of their replacement through comprehensive flow analyses. The results emphasise the importance of analysing jet flow, vortical structures, momentum balance and vorticity transport for evaluating aortic valve performance.

Main

Aortic stenosis (AS) concerns the progressive deterioration and remodelling of the leaflet tissue, which reduces its dynamics. This leads to an increased resistance for the blood to flow from the left ventricle to the aorta, especially during systole, and to the possibility for blood to flow back during diastole[8,9,38]. The long-term consequences of such a pathology are very serious including heart failure and mortality is more than 90% within a few years after the onset of symptoms[34]. Valvular prostheses made from either rigid materials such as titanium or carbon, known as mechanical heart valves, or from biological tissue, known as bioprosthetic aortic valves (BioAV), have become a common solution for replacing the diseased aortic valve through a procedure called aortic valve replacement (AVR). AS prevalence increases with age and affects as many as 5% of the population after 75 years of age. AS is responsible for 300,000 surgical aortic valve replacements worldwide annually, a number that is expected to double by 2050 with the ageing population[28].

The performance of aortic valves surgically implanted and made from biological tissue such as porcine or bovine pericardium has been extensively investigated in the literature[2,3,8,38] but the link between valve design, flow features and leaflet motion has never been studied whether experimentally or computationally.

Bescek *et al.*[3] presented a computational characterisation of the turbulent features of the flow downstream of one bioprosthetic aortic valve model under peak systolic conditions. To do so, they performed a statistical analysis on the flow data and found that the total rate of turbulent dissipation was responsible for 26% of the total pressure loss across the valve indicating that turbulence is a significant and detrimental factor for haemodynamic performance. They also noted that the shedding of vortex rings periodically generated at the leaflet tips at a frequency of 36 Hz as a consequence of the periodic leaflet motion leads to peaks of viscous shear stresses, Reynolds' stress and dissipation rate of turbulence at a distance of 30 mm from the leaflet tips. However, in their study, Becsek *et al.*[3] did not analyse the downstream evolution of vortices from the specific aortic valve bioprosthesis under consideration. They also did not establish a connection between valve design, leaflet

motion, the observed vortical structures and the spatial-temporal variations in vorticity. Furthermore, they did not quantify the drag forces associated with the presence of the mentioned bioprosthetic aortic valve.

Furthermore, Johnson *et al.*[21] studied the impact of heart valve tissue thickness on the presence, nature and extent of leaflet flutter. Under the assumption that the cyclic-strain behaviour observed when valve leaflet free edge flutters over the lifetime of the valve causes an additional induced cyclic loading that may contribute to non-uniform or accelerated leaflet fatigue and deterioration, their study demonstrated that a major reduction in valve material thickness can induce detrimental leaflet flutter. Relying upon an immersogeometric analysis framework to simulate the fluid-structure interaction problem and on a flutter-quantification methodology, their results exhibited the impact that a single parameter can have on both the structural performance of the tissue and the blood flow behaviour throughout the whole cardiac cycle. Nevertheless, flow quantities related to turbulence were not calculated and the conclusions as to the impact of the flutter motion on the flow was limited to the visualisation of iso-surfaces of instantaneous velocity and vorticity field close to the valve and in the curved ascending aorta model.

Most recently, Morany *et al.*[25] conducted a computational study of the fluid-structure interaction problem arising in healthy tricuspid and biscuspid aortic valves (TAV and BAV). For this purpose, they strongly coupled, using a partitioned approach, the lattice Boltzmann method (LBM) to solve the blood motion equation to a Finite Element (FE) method to solve the elastic body motion equation. To model the constitutive relationship of the porcine leaflets, they considered a symmetric collagen fibre network (CFN) embedded in an elastin matrix for each valve leaflet. The distribution of these fibres was obtained by averaging the maps of fibre bundles observed under a microscope for 15 porcine leaflets[23]. Morany *et al.* concluded that their LBM-FE FSI approach was able to reliably assess velocity, and more specifically the velocity oscillations occurring at mid-diastole downstream of the TAV, and wall shear stress throughout the whole cardiac cycle in the vicinity of a TAV and a BAV. To state this, they conducted a comparison by evaluating the range of maximum

velocity achieved in the jet issuing from the leaflets at systole peak and compared it to values documented in existing literature. Additionally, they compared the wall shear stress values on the ventricular side of the leaflets during leaflet coaptation and at systole peak with the range of values reported in previous studies. However, it is important to note that the comparison was limited to expected ranges of values and no detailed examination of spatial distributions for both velocity and wall shear stress fields was carried out. Furthermore, the resolution of the fluid lattices considered in Morany *et al.* only permitted the analysis of large-scale flow features, thus neglecting the small-scale velocity fluctuations that are of great importance when characterising the transition to turbulence in the aorta.

The present work is the first part of a comprehensive two-part study. In this work, the analysis of blood motion focuses on characterising flow topology by describing the distribution of velocity magnitude and the dynamics of coherent vortical structures downstream of three different valvular configurations. The temporal evolution of the terms of the vorticity dynamics equation is also investigated. Besides, two novel quantities corresponding to the vortex advection and stretching terms, projected onto the eigenbasis of the vorticity gradient and rate-of-strain matrices, respectively, are introduced.

To the best of our knowledge, a comprehensive computational study and detailed analysis encompassing various designs of aortic valve bioprostheses along with a comparative analysis to a severe stenotic case have not been previously undertaken. This work makes a significant contribution to the advancement of optimally designed and patient-customised aortic valves. Through dedicated flow analysis, it comprehensively investigates the flow topology near a pathological aortic stenosis, comparing it to the flow characteristics downstream of two surgical valve bioprostheses. These two bioprostheses have undergone modifications in their leaflet geometry by changing thoughtfully selected geometric parameters. The connection between the two valve designs, subsequent leaflet motion and encountered aortic flow features is established.

Jet flow topology

Fig. 1 presents the velocity magnitude in a plane at a distance of 10 mm from the STJ (plane 1) as well as the evaluation of the eccentricity of the jet centre (white dots in Fig. 1) in relation to the centre of the circular cross-section (black dot in Fig. 1).

In the stenotic case, the eccentricity angle α_c of -5° to 5° and eccentricity distance ε_c of about 2 mm do not significantly vary over time as the orifice geometry is immobile due to the calcified leaflets (see Fig. 5 (f)). Moreover, the regions situated between commissures 1-2 and 2-3 (cf. Fig. 1) exhibit elevated velocity magnitudes that extend from the jet, in contrast to the region between commissures 1-3. This trend is further highlighted in Fig. S4 of the supplementary material illustrating vortex stretching magnitude in the proximal plane p1. In fact, we observe that elevated values of vortex stretching magnitude are predominantly located between commissures 1-2 and 2-3. Conversely, within the area between commissures 1-3, the magnitude of vortex stretching is negligible. At time instant t=0.12 s, the velocity magnitude in the trilobal jet drops, which is represented by a 30% decrease in the maximal velocity magnitude. The corresponding shear layers present smaller velocity gradients at this instant and are thicker. In Fig. S4, this trend is indicated by a decrease in the vortex stretching magnitude. From 0.21 s until 0.3 s, the velocity magnitude in Fig. 1 indicates a more ordered separation between the main high velocity jet flow and the surrounding secondary low velocity flow. In Fig. S4 and Fig. 4 (a), this is revealed by a decrease in the values of $||S_{\boldsymbol{\omega}}||$ over the proximal plane or averaged over the volume of investigation (VoI).

Concerning the VLth30 BioAV case, the eccentricity distance and angle vary throughout the systolic phase with higher eccentricity distances observed from t=0.21 s onward. This is a direct consequence of the three leaflets moving asymmetrically with a displacement magnitude amplitude of 1.5 to 2 mm (see Fig. S1 in the supporting information). From Fig. S1, it is also noteworthy that the amplitude and difference in the three leaflets' position in relation to their initial position is more pronounced from t=0.21 s onward. Besides, as compared to the stenotic case, the motion of the leaflets and of the connected flow motion leads to a 10 to 20% smaller maximum velocity in the jet reaching peak values between

t=0.12s and t=0.15s as shown in Fig. S2 (a). The velocity magnitude distribution in the region surrounding the jet is much less organised and presents larger velocity values as compared to the stenotic case due to the leaflet motion pushing blood in this region and promoting mixing of high and low velocity zones.

With regard to the Ulth0 bioprosthesis case, given the almost immobile leaflets at peak systole (see Fig. 8 (c) and Fig. S1), the eccentricity distance ε_c is negligible. The shape of the jet is well defined and triangular. Between time instants t=0.15 and t=0.21 s, an instability is observed in the shear layer between the high-velocity jet (with a maximum velocity of 2 m/s, as shown in Fig. S2 (a)) and the surrounding quiescent region. This instability is characterised by the emergence of wavy irregularities in the velocity distribution at the borders of the triangular jet. It arises from the entrainment of high-velocity fluid elements into the region of lower velocity, subsequently pushing the low-velocity fluid towards the high-velocity flow region. This change in the velocity distribution and the creation of vortices along the shear layer interface is known as the Kelvin-Helmholtz instability (KHI)[14]. In the Ulth0 case, this instability, which breaks the flow axisymmetry, is likely to be accentuated by the flow deceleration that begins at t=0.1 s and is imposed by the inflow conditions (see Fig. 7).

Finally, it is of relevance to mention that the fixed triangular-shaped jet described in the Ulth0 valvular case issuing from the valve leaflets has been also noted in Corso *et al.*[8] throughout systole and by means of three-dimensional particle tracking velocimetry measurements, downstream of a Medtronic (Minneapolis, Minnesota, USA) Evolut R transcatheter aortic valve. In the study by Corso *et al.*[8], another transcatheter valve, namely the CoreValve from Medtronic, was tested. Worthy of noting that the phase-averaged flow analysis revealed a jet of moderate velocity with an elliptical shape, the position of which varied in relation to the aorta wall during systole. This observation is congruent with the moving jet of moderate to high velocities noted for the VLth30 valvular case characterised by a varying eccentricity distance and angle of the jet over systole.

[Figure 1 about here.]

The velocity magnitude in a distal plane (at a distance of 24 mm from the STJ) is presented in Fig. 2. In the stenotic case, the stratified organisation between two clear flow zones, i.e. a trilobal jet of high velocities and the surrounding quiescent flow, is not present anymore. Instead, scattered high velocity patches resulting in longer and disorganised shear layer interfaces are pushed toward the outer wall of the aorta model from t=0.12 s. We speculate that the shift of the high velocity jet toward the outer wall results in the impingement of the vortices against the wall leading to a break-up of these vortices. In addition, the separation between a helical flow motion in the time-averaged velocity field along the inner wall[10] and the shattered initial jet along the outer wall creates at the interface between these zones a sustained entrainment of fluid momentum in the high velocity zone. Concerning the VLth30 case, the jet flow structure with the moving high velocity region is still noticeable and the maximum velocities in the distal plane p2 are similar to the ones encountered in the proximal plane p1. The most striking features in the distal plane are the thickening of the interface between the high flow regions, corresponding to the tail of the jet and the low flow regions resulting in smaller velocity gradients at the shear layers. Furthermore, the time-varying position of the jet tail follows the one remarked in the proximal plane through the analysis of jet eccentricity emphasising the importance of leaflets' motion effect also on distal flow structures.

In the Ulth0 BioAV case, similarly to the case with the VLth30 BioAV, the central jet can still be observed in the distal plane. Unlike the well defined triangular jet noted in the proximal plane, irregularities and thickening of the shear layer interface are observed at all the time instances over systole as a result of the shedding of the vortices created in the shear layers upstream.

[Figure 2 about here.]

Vortical structures

In Fig. 3, the image sequence of the intricate coherent vortical structures downstream of the aortic stenosis and the two BioAVs is visualised using the λ_2-criterion[20].

In the stenotic case, we note a starting vortex ring hugging the shape of the stenotic orifice. The high difference in velocity between the accelerating flow (maximum velocity in the stenotic jet of 1.9 m/s) and the quiescent flow close to the wall of the aorta brings about zones of high shear at the interface propitious for the roll-up and shedding of eddies. This initial vortical structure is then shed and broken into smaller vortices that occupy the whole straight aorta volume under the push of a high velocity jet. From time t=0.09 s onward, due to the impingement of the jet on the outer wall of the curved ascending aorta, as presented in Corso *et al.*[10], a secondary retrograde helical mean flow motion with smaller velocities is created in the curved portion of the aorta and pushes the majority of the vortical structures towards the outer aortic wall accentuating the asymmetry in the spatial distribution of the vortical structures. The high velocity jet is thus confined in the outer wall region throughout the whole systole. At the interface between the high-velocity jet and the low-flow regions near the inner wall, the entrainment of fluid with low momentum at the shear layers leads to intermittent increases in the number of small-scale densely distributed vortices at times t=0.12, 0.18, 0.21, and 0.27 s. This intermittent surge in vortex break-up is mainly located close to the outer wall. The times at which it occurs coincide with the time instants at which slightly decelerating inflow velocities upstream of the stenosis are imposed (see Fig. 7).

With regard to the VLth30 BioAV case, initial coherent vortices are found along the free edge of the leaflets (t=0.03 s). These vortices quickly dissipate due to leaflet motion. However, starting at t=0.03 s, new vortical structures resembling hairpin vortices (as seen in the inset of Fig. 3 at t=0.06 s) form in the gaps between the leaflet commissures and above the ring posts. In fact, the movement of the ring posts, resulting from the unstable motion of the leaflets, initiates the generation of hairpin-like vortical structures, particularly when the gaps widen. At t=0.09 s, we note large vortical structures stretched in the axial direction issuing from the moving leaflet free edges. Between t=0.12 and 0.21 s (after the inflow conditions

reach the peak flow), due to flow deceleration, the coherent vortical structures are broken down into small vortices uniformly distributed over the whole straight ascending aorta as a consequence of the moving leaflets and valve orifice promoting higher mixing and vortex merging further downstream. Besides, large coherent eddies are displayed close the leaflet free edges and in the low velocity regions whereas stretched and smaller eddies are found in the shear layers, i.e. at the interface between the high velocity jet and the surrounding quiescent fluid close to the aorta wall. Between t=0.24 s and t=0.3 s, the breakdown of the vortex is diminished as compared to previous times due to a reduction in jet velocity. However, the presence of large-scale vortical structures, induced by the motion of the leaflets, is still observable.

In the Ulth0 BioAV case, a pattern reminiscent of the VLth30 case emerges, characterised by an initial vortex ring at the leaflets' free edge. It is interesting to note that up until t=0.06 s, the jet of fluid maintains a circular shape, aligning with the contours of the orifice. Due to the flow acceleration, beyond t=0.06 s, the shape of the jet becomes triangular. The initial vortex ring sheds and fades after t=0.03 s owing to the formation of new eddies at the the ring posts. In fact, akin to the VLth30 BioAV case, hairpin-shaped vortices are found at the ring post at t=0.06 s due to the commissural gap between the leaflets (see inset at t=0.06 s in Fig. 3). Unlike the other BioAV case though, between t=0.12 s and t=0.21 s, these hairpin-shaped vortices demonstrate a tendency to elongate axially before being broken down into smaller vortices further downstream. This change in vortex shape is instigated by heightened shear between the triangular jet of elevated velocities (peaking at 1.8 m/s) and the surrounding zones of low velocity. Consequently, the presence of the three ring posts under stable leaflet motion condition, as the one observed in the Ulth0 BioAV case (cf. Fig. 8 (c)), has a pivotal influence on the distribution and size of the vortices downstream of the valve. From t=0.21 s onward, the number of coherent vortical structures dwindles as a result of the flow deceleration as illustrated in Fig. 7.

[Figure 3 about here.]

Momentum balance

To compare the results downstream of the three valvular configurations examined in this study with the findings of Chen and Luo[7] and Becsek *et al.*[3] and to evaluate the flow resistance resulting from the presence of prosthetic or stenotic valves, we compute each term of the flow momentum balance in the streamwise direction within a control volume, V_{con}, which corresponds to the fluid present in both the ascending aorta and the sinus. The examined quantities, derived from the momentum balance equation and non-dimensionalised using the maximum pressure flux difference over systole, are listed below and presented in Table 1:

- the pressure term ΔPA averaged over the systole;
- the acceleration term $\dot{p} = \frac{\partial}{\partial t} \iiint_{V_{con}} \rho u_z \, dV$ averaged over the systole with V_{con}, the control volume;
- the mean and maximal drag coefficient $C_D = (2F_{\texttt{leaflets}}) \,/ \left(\iint_{in} \rho u_z^2 dA \right)$ with $F_{\texttt{leaflets}}$, the total hydrodynamic force acting on the leaflet surfaces and the denominator being the inlet momentum flux;
- the mean equivalent length of accelerated fluid column $h_{F_{\texttt{leaflets}}} = (LF_{\texttt{leaflets}}) \,/\dot{p}$ made dimensionless by dividing it by the reference diameters $\varnothing_{\texttt{sten}} = 0.011$ m and $\varnothing_{\texttt{BioAV}} = 0.018$ m. L is the length (in the Z-direction) of the control volume.

Table 1 shows that the time-averaged dimensionless pressure flux difference is of a comparable magnitude for the bioprosthetic cases (lines 2, 3, 4 in Table 1) and the flexible aortic valve case (line 5 in Table 1) but it is 67% higher in the stenotic case. This larger value can be attributed to stenosis, which introduces larger pressure loss as well as to the curved aorta geometry in the stenotic case, which modifies the position where pressure recovery arises[36]. In addition, in the stenotic case, the time-averaged acceleration term is two to four times as small as that calculated in the four prosthetic aortic valve cases.

With regard to the drag coefficient C_D, the mean and maximal values for the cases presented

in Becsek *et al.* (line 4 in Table 1) and Chen and Luo (line 5 in Table 1) are in good agreement. This can be attributed to the observed strong periodic flutter of the leaflets[3,7]. This type of flutter motion leads to the generation of a sequence of vortex rings, whose shapes vary over time[7]. For the other two BioAV cases studied in this work (lines 2 and 3), the drag coefficient (C_D) values are one-fourth to one-fifth of those calculated from the data presented in[7] and[3]. The VLth30 case presents higher C_D value compared to the Ulth0 case as a consequence of the non-axisymmetric but moderate flutter motion (see Fig. S1 in the supplementary information). This underscores the influence of leaflet geometry on the resistive forces introduced by the aortic valve prosthesis and its correlation with the type of flutter motions exhibited by the leaflets.

In relation to the equivalent length of the fluid column $\overline{h_{F_{\texttt{leaflets}}}}$ decelerated due to the reaction forces at the leaflet surfaces, the stenotic case displays the highest value. However, for the valvular cases demonstrating periodic flutter of the leaflets with substantial displacement magnitudes (lines 4 and 5 in Table 1), the decelerated fluid column due to the presence of the valve falls within a similar range as that observed in the case of aortic stenosis for the flexible valve scenario presented by Chen and Luo[7] and is 50% smaller in the case investigated by Becsek *et al.*[3]. The newly designed BioAV cases, namely VLth30 and Ulth0, exhibit values for $\overline{h_{F_{\texttt{leaflets}}}}$ that are 4 and 6 times smaller than the value calculated in the stenotic case, respectively.

[Table 1 about here.]

Vorticity transport and vortex stretching

Finally, we analyse the vortex stretching term $S_{\boldsymbol{\omega}}$ and advection due to the flow velocity $A_{\boldsymbol{\omega}}$ of the vorticity transport equation (cf. Eq. 2). This transport equation is central for the characterisation of the evolution and distribution of vortices, especially pertaining to their amplification or decay at the considered time instance.

In Fig. 4 (a), the evolution of the magnitude of the vortex stretching tensor averaged over

the VoI is presented. In the stenotic case, $< ||S_{\boldsymbol{\omega}}|| >$ generally decreases over systole with 5 peaks occurring at t=0.125, 0.143, 0.193, 0.25 and 0.28 s. The peaks observed, ranging between 1.85×10^5 and $2.8 \times 10^5\ s^{-2}$, correspond to instances when a higher density of vortical structures were identified in Fig. 3.

In the VLth30 case, between t=0.135 s and 0.156 s, peak values of $1.76 \times 10^5\ s^{-2}$ are exhibited following the trend of the inflow rate time series consisting of an acceleration until t=0.1 s and a two-third less deceleration until t=0.21 s (cf. Fig. 7).

In the Ulth0 case, a peak value of $1.38 \times 10^5, s^{-2}$ is observed at t=0.186 s. The rate of change over time for the vortex stretching magnitude in this case is nearly identical. Finally, the time-averaged $< ||S_{\boldsymbol{\omega}}|| >$ presented in the table of Fig. 4 (d) is twice as large for the stenosed aorta case compared to the values calculated in the two BioAV cases.

The time series of the ensemble-averaged projected vortex stretching as defined in Eq. 3 is shown in Fig.3 (b). It is noteworthy that the majority of values are highly positive in the case of calcific stenosis, especially up to t=0.23 s. Positive projected vortex stretching reaching a maximal value of $1.33 \times 10^4\ s^{-2}$ in the stenotic case suggests an alignment of the vorticity vector and the principal directions of the rate-of-strain tensor multiplied by the eigenvalues of this tensor. It represents a phenomenon called vorticity amplification or intensification[37] characterised by the elongation of vortical structures and an increase in the rotational motions in the flow. In the VLth30 bioprosthetic case, positive levels of $< \Pi^{S_{\boldsymbol{\omega}}} >$ are found between t=0.11s and 0.156s and between t=0.19 s and 0.22 s with a maximum of $3.5 \times 10^3\ s^{-2}$ and on average over systole, the projected vortex stretching is positive (see Fig. 4 (d)). In contrast, the levels of $< \Pi^{S_{\boldsymbol{\omega}}} >$ for the Ulth0 case are mainly negative. This results, as shown in the table of Fig.4 (d), in a negative time-averaged value, which is 4.7 times smaller in magnitude than that for the stenotic case and 4.4 times larger than the one obtained for the VLth30 BioAV case. It is worth noting that negative projected vortex stretching is associated with an anti-parallel alignment of the vorticity vector and the strain rate, resulting in a decrease in overall vorticity acceleration, a phenomenon known as vorticity attenuation[37]. This attenuation is linked to the favourable reorganisation of the

flow and the suppression of flow disturbances.

Fig.4 (c) shows the time evolution of the projected vorticity advection, which represents the intensity whereby vorticity is transported by the velocity field. In fact, a positive (negative) value indicates that the velocity vector is parallel (anti-parallel) to the principal directions of the vorticity gradient tensor and the magnitude is the result of the multiplication of the latter by the eigenvalues of the vorticity gradient tensor. In other words, positive ensemble-averaged projected vorticity advection values indicate that spatial variations in the vorticity field primarily occur along the flow direction, while negative values suggest that the deformation in the vorticity field predominantly opposes the flow direction. For the aortic valve stenosis case, we observe that $< \Pi^{A_{\boldsymbol{\omega}}} >$ levels are, for the most part of systole, positive leading to a large time-averaged value of 9,157 s^{-2} as shown in the table of Fig. 4 (d). We also note that this time-averaged $< \Pi^{A_{\boldsymbol{\omega}}} >$ is 3.65 times as large as the time-averaged $< \Pi^{S_{\boldsymbol{\omega}}} >$ and of the same sign. Concerning the VLth30 bioprosthetic valve case, $< \Pi^{A_{\boldsymbol{\omega}}} >$ alternates between positive and negative values over systole resulting in a negative time-averaged value. The times at which these negative and positive peaks occur are coincident with the times of the peaks observed in Fig. 8 (c) and Fig. S2 for the area at the vena contracta and vorticity deficit, respectively. Thereby, the asymmetric leaflet motion does play an important role in the transport of vortices in the region downstream of the valve albeit not necessarily by promoting the advection of the vorticity field in the flow direction but in an opposite direction as well. Finally, the magnitude of time-averaged $< \Pi^{A_{\boldsymbol{\omega}}} >$ is in this case 2.8 times as large as as the time-averaged $< \Pi^{S_{\boldsymbol{\omega}}} >$. For the Ulth0 case, the most favourable conditions are met to fulfil vorticity weakening in the bulk of the flow downstream of the valve with a positive time-averaged $< \Pi^{A_{\boldsymbol{\omega}}} >$, whose magnitude is 26% less than the magnitude of time-averaged $< \Pi^{S_{\boldsymbol{\omega}}} >$. As previously stated, the latter is negative highlighting a more pronounced vorticity attenuation over the VoI.

[Figure 4 about here.]

Outlook

These findings emphasise the complex interplay between valve geometry, leaflet motion and aortic haemodynamics. They highlight the importance of understanding jet flow topology, vortical structures close to the valvular orifice and of analysing momentum balance and vorticity transport for assessing the performance of aortic valves.

In fact, the comprehensive analysis conducted in this first part of the study contributes to our understanding of the critical geometrical features of valve design that promote a more organised and physiological flow. This, in turn, leads to a reduction in pressure loss and decreased haemodynamic forces acting on blood cells and on the aortic wall.

The two-part computational study, which comprehensively analyses aortic flow data, paves the way for the development of innovative and patient-customised valve designs that can optimise systolic flow patterns and minimise detrimental effects associated with aortic valve replacement.

Methods

Geometrical models and leaflet geometry parametrisation

As far as the severely calcified aortic valve case is concerned, the geometry of the curved aorta was obtained from an MRI scan (cf. Fig. 5 (a, b)) and has a diameter at the sino-tubular junction (STJ) d_{STJ}^{sten} of 25 mm (see Fig 5 (e)). A patient-based geometry of stenosis was added to the sino-tubular extremity and the eccentric stenotic orifice subsequent to the calcification of a tricuspid aortic valve is shown in Fig. 5 (f). The reduction in cross-sectional area through the orifice is about 80%[9,10]. Within the scope of this study, only the straight section of the ascending aorta is considered when comparing the jet flow structures present in the vicinity of the orifice for the stenotic and bioprosthetic cases (see Fig. 5 (b, c)).

Concerning the bioprosthetic valve cases, the geometry of the aortic root (AR) including the sinus of Valsalva (SOV) geometry is similar to the one presented in Bescek *et al.*[3]. The

main dimensions of the sinus portion and the straight aorta are shown in Fig. 5 (g, h). The geometry of the bioprosthetic heart valves, including three leaflets and a supporting ring, corresponds to an approximate reproduction of the commercial valve *Edwards Intuity Elite 21mm* (Edwards Lifescience, Irvine, CA, USA). The leaflets are made from glutaraldehyde-fixed bovine pericardium and are mounted on a rigid ring made of polymer supported by a nitinol wireframe and covered with fabric. The BioAV models are introduced in the AR, as shown in Fig. 5 (d).

[Figure 5 about here.]

To test the influence of different leaflet geometries of BioAV on their kinematics and on the flow characteristics at peak systole, two new geometrical configurations (with reference VLth30 and Ulth0) for the 500-micron-thick leaflets have been designed (cf. Fig. 6 (b, c)). Besides, it is assumed that the designed initial leaflet position corresponds to the stress-free configuration. As shown in Fig. 6 (b) and (c), the two geometries of the newly designed leaflets vary with each other based on three features of the leaflet: (i) the belly curve, i.e. the curve obtained by longitudinally cutting the leaflet in half (cf. Fig. 6 (b, c, e) ; (ii) the free edge, i.e. the leaflet extremity not attached to the ring (Fig. 6 (a)); (iii) the scallop or attachment curve, i.e. the leaflet extremity attached to the ring (Fig. 6 (d)). Each feature of the designed leaflets is defined based on different parameters that are summarised in Fig.6 (f). The belly curve with centred and normalised coordinates is defined by two parameters a and b of the hyperbolic sine function as shown in Fig.6 (e). Depending on the geometry of the ring and on the other two features, the belly curve is dimensionalised leading to two radial lengths (ΔX_{Ulth0}, ΔX_{VLth30}), two axial lengths (Δh_{Ulth0}, Δh_{VLth30}) and two belly curve lengths ($l = 13\ mm$ and $L = 14.5\ mm$).

The free edge is characterised by the angle θ between the plane perpendicular to the centreline of the straight aorta passing through the intersecting points of the free edge and scallop curve and the plane defined by the centre point of the free edge and the intersecting points of the free edge and scallop curve.

The shape of the scallop curve of the leaflets to the valve ring is classified as V- or U-shaped depending on its resemblance to the corresponding letter.

[Figure 6 about here.]

The following nomenclature consisting of a sequence of letters and digits is used to refer to the two leaflet geometries: attachment curve shape - length of the belly curve - th - value of θ (cf. Fig. 6 (b, c, f)).

Numerical setups

The direct numerical simulation (DNS) of blood flow in the stenosed aorta was conducted with the open-source code NEK5000[26]. This code is based on a spectral element method[13] solving the Navier-Stokes equations for Newtonian and incompressible flows. Details on the numerical methods used and on the implementation of the direct numerical simulation can be found in Corso *et al.*[9]. It is worth noting that the Reynolds number Re_o calculated at the stenotic orifice averages at 3,800 over systole. Re_o is determined by considering the diameter of the circular area corresponding to the stenotic orifice area and the spatially averaged velocity at the orifice. The Dirichlet inflow boundary conditions on the three components of velocity over the inflow cross-section upstream of the stenosis are prescribed such that pseudo-steady systolic conditions (taking into account flow variations measured during *in vitro* experiments) are simulated reaching a mean systolic flow rate of 12 L/min[9,10] (cf. Fig. 7).

With respect to the simulation of the bioprosthetic aortic valve cases, the computational method for the high-fidelity simulation of the blood flow and the mechanics of the leaflets relies on a fluid-structure interaction (FSI) approach based on a modified immersed boundary method taking into account a deformable structure (i.e. the valve and the aorta) embedded into a fixed fluid domain[31,27].

The Navier-Stokes equations for incompressible flows of Newtonian fluid are solved on a Cartesian grid (of dimension 40 x 40 x 80 $[mm^3]$ with 120 x 120 x 288 points for each direction)

using sixth-order compact finite differences on staggered grids for each velocity components and pressure[35]. Grid stretching is applied so that the cell dimension close to the jet shear layers is about 100 μm. Moreover, an explicit low-storage third-order accurate Runge-Kutta time stepping scheme for the advective term and a semi-implicit Crank-Nicolson scheme for the temporal discretisation of the diffusive term[17] are used. An iterative solution technique was developed to solve the large linear system of discretised equations for the fluid sub-problem[17]. This technique is based on the Schur complement formulation of the original linear system and relies on the resolution of two Poisson problems on pressure solved with the Krylov subspace bi-conjugate gradient stabilised method (BiCGstab) with right preconditioning (geometric multigrid V(3,3)-cycle scheme as a preconditioner). A dedicated highly efficient commutation-based preconditioner matrix is indeed applied for the pressure iterations[17,24]. A Helmholtz problem on velocity is then solved with the unpreconditioned BiCGstab method. The termination of the Helmholtz iterations and the convergence of the residuals in order for the continuity constraint to be met is controlled through an absolute threshold parameter $\varepsilon_U = 10^{-10}\ m/s$ or s^{-1} while the accuracy level in the Poisson iterations is dependent on the supremum norm of residuals out of the velocity divergence computation between two consecutive iterates and a tolerance value set to 10^{-4} [17]. The presented Navier-Stokes solver was tested for transitional and turbulent channel flows and the accuracy of the solver was verified by comparing the results with solutions from a pseudospectral solver[17]. Direct numerical simulation of transitional blood flow in the straight ascending aorta for the two valvular cases is then considered in this study.

The elastodynamics equation is solved on a moving tetrahedral mesh (i.e. on a Lagrangian frame of reference) of about 200,000 affine elements using the finite-element formulation and a second-order accurate semi-implicit central difference time-stepping scheme[27,30,35]. All the structural parts (i.e. aorta, leaflets and ring) share element nodes at their intersection. The Newton method is used to linearise the system of non-linear equations for the solid sub-problem and the linear system of equations is solved using a generalised minimal residual iterative method (GMRES) with an additive Schwarz preconditioner[30,33]. The relative and

absolute tolerance value on the residuals to stop the iterations for the resolution of the linear and non-linear systems is set to 10^{-6} and 10^{-8}, respectively[3].

The strong coupling of the Navier-Stokes and elastodynamics equations is based on a parallel variational transfer[22] of velocities (from fluid grid to solid mesh) and of reaction forces (from solid mesh to fluid grid) between non-matching discretisation points and elements' nodes. The fluid and solid sub-problems are solved synchronously with a time-step of 5×10^{-6} s. The formulation of the variational transfer corresponds to the equalities of the L^2-projections of velocity or forces between two non-overlapping meshes by defining a suitable space of Lagrange multipliers. The transfer operator is then assembled from mortar matrices computed by numerically integrating the Lagrange basis functions of the three spaces. A linear system is ultimately solved to obtain the projected velocities imposed as Dirichlet boundary condition at the fluid-structure interface of the solid sub-problem and the projected force density added as a source term to the blood flow momentum equation. An iterative procedure, stopped when a prescribed relative tolerance of 10^{-6} is reached, is implemented to ensure velocity and force continuity at the fluid-structure interface[27,22].

Concerning the material properties for the structural elements of the investigated FSI problems, a fibre-based model is used to characterise the nearly incompressible anisotropic material properties of the glutaraldehyde-pretreated bovine pericardium leaflets[1,18,27,35]. The six parameters of this constitutive model, including two families of fibres oriented at a fitted angle of 60° to each other, were regressed to match experimental bi-axial tensile test data[1]. The material properties of the aortic wall and the supporting ring of the leaflets are described by a linear elastic constitutive relationship (density: $1500 kg/m^3 (ring)$; 1100 kg/m^3 (leaflets, aortic root and aorta), bulk modulus: 3 MPa and shear modulus: 0.3 MPa)[3]. Following a well-established assumption[5], blood is modelled as a Newtonian fluid with a constant kinematic viscosity ν of 3.77×10^{-6} m^2/s, equal to the blood viscosity in the ascending aorta at the largest shear rate and a density ρ_f of 1060 kg/m^3.

Systolic flow conditions are considered in the computational study. A pressure drop across the valves and in the ascending aorta of 8 mmHg is imposed over a time span of 0.3 s[35]. In

order to prescribe a pressure difference within a cylindrical region upstream of the valve[35], which corresponds to the left ventricle outflow tract (LVOT), a forcing term is introduced on the right-hand side of the fluid momentum equation. This method is adapted from the concept of fringe regions or sponge layers as described in[4,6]. Consequently, the inflow velocity undergoes gradual acceleration due to the pressure difference imposed by means of the additional forcing term given by the following equation:

$$\mathbf{f}_{inflow} = \begin{bmatrix} \frac{\lambda(l)}{\lambda_{max}} \frac{\Delta p_{inflow}}{h_{\mathtt{cyl}}} \frac{1}{\rho_f U_{\mathtt{ref}}^2} \\ \lambda(l)\,(0 - u_2/U_{\mathtt{ref}}) \\ \lambda(l)\,(0 - u_3/U_{\mathtt{ref}}) \end{bmatrix} \; [-] \tag{1}$$

where $\lambda(l)$ is a damping function vanishing in the physical domain, flat in most of the interior of the cylindrical fringe region, while decaying smoothly to 0 at the boundaries of the fringe region[6]. λ_{max} is the magnitude of the damping function. Δp_{inflow} is equal to 16 mmHg (= 2133.2 Pa). $U_{\mathtt{ref}}$ is the reference velocity used to non-dimensionalise the velocity vector $\mathbf{u}$ in the Navier-Stokes equations. $h_{\mathtt{cyl}}$ is the length of the cylindrical fringe region. A coordinate system projection is performed such that the pressure difference imposed by $\mathbf{f}_{inflow}$ along direction l aligns with the normal to the inflow cross-section and in the streamwise direction. u_2 and u_3 are then the velocity components perpendicular to the axis of the cylindrical fringe region.

In addition, a second cylindrical fringe region is positioned at the outflow extremity of the aorta model. Its purpose is twofold: firstly, to emulate the resistance (by applying a resistive pressure) arising from the curved portion of the aorta (which is not modelled in the pericardial bioprosthesis cases) and secondly, to attenuate the flow fluctuations that might otherwise flow back due to the periodic boundary conditions prescribed on the fluid Cartesian grid[35]. The expression governing the forcing term in the second cylindrical fringe region shares a similar form with Eq. 1, except that $\Delta p_{outflow}$ is set to -8 mmHg (= -1066.6 Pa).

A third cylindrical fringe region cancelling out the radial velocity components with a reduced width and placed before the inflow fringe region is finally added from time instant 0.1 s onward (after reaching a peak flow rate of about 16 L/min[8]) to model the gradual

flow deceleration occurring from time instances 0.1 s to 0.3 s (see Fig. 7). Similarly to the simulation setup for the aortic stenosis case, the reference Reynolds number at the valvular orifice Re_o is equal to 3,800 in the BioAV cases. This Re_o corresponds to the Reynolds number computed by taking the average velocity at the valvular orifice and the diameter of the circular area corresponding to the BioAV orifice area over the acceleration and deceleration phases occurring throughout systole (see Fig. 7). These phases result from the use of the three fringe regions.

[Figure 7 about here.]

Vortex structures, dynamics, stretching and circulation

The instantaneous vorticity transport equation, which is obtained by taking the curl of the three-dimensional momentum Navier-Stokes' equation and using vector identities, is:

$$\frac{D\boldsymbol{\omega}}{Dt} = \underbrace{\frac{\partial \boldsymbol{\omega}}{\partial t}}_{L_{\boldsymbol{\omega}}} + \underbrace{\mathbf{u} \cdot \nabla \boldsymbol{\omega}}_{A_{\boldsymbol{\omega}}} = \underbrace{\boldsymbol{\omega} \cdot \mathbf{L}}_{S_{\boldsymbol{\omega}}} + \underbrace{\nu \nabla^2 \boldsymbol{\omega}}_{D_{\boldsymbol{\omega}}}. \tag{2}$$

with $L_{\boldsymbol{\omega}}$, the local vorticity acceleration, $A_{\boldsymbol{\omega}}$, the vorticity advection; $S_{\boldsymbol{\omega}}$, the vorticity stretching and $D_{\boldsymbol{\omega}}$, the vorticity diffusion. Of particular interest in this study is the vortex stretching term as the latter represents the rotational acceleration (or deceleration) brought about due to strain $\mathbf{L}$ parallel (or anti-parallel) to the vorticity vector $\boldsymbol{\omega}$. As shown in Eq. 2 for three-dimensional viscous flows, the rate of change of vorticity is dependent on both the stretching and diffusion terms. In fact, a high and positive stretching term increases the rate of change of vorticity (phenomenon called amplification) and because of the conservation of the angular momentum, vortex filaments are confined as a consequence of the decrease in the coherent vortex radius.[32]. At moderate Reynolds numbers, the diffusion term is predominant in the smallest length scales of the flow except at the wall where viscous forces dominate.
The magnitude of the advection $A_{\boldsymbol{\omega}}$ and stretching terms $S_{\boldsymbol{\omega}}$ is investigated. Nonetheless, in order to take into account the orientation of both the rate of strain in the blood flow in relation to the vorticity vector, a projected vortex stretching $\Pi^{S_{\boldsymbol{\omega}}}$ is introduced and defined as

the vorticity vector projected onto the eigenvectors of the rate-of-strain tensor and multiplied by the eigenvalues of this tensor:

$$\Pi^{S_\omega} = (\boldsymbol{\omega} \cdot \mathcal{V}_{\mathbf{L}}) \cdot \boldsymbol{\lambda}_{\mathbf{L}}, \tag{3}$$

with $\mathcal{V}_{\mathbf{L}}$, the eigenvectors of $\mathbf{L}$ and $\boldsymbol{\lambda}_{\mathbf{L}}$, the eigenvalues of $\mathbf{L}$.

A similar definition is used to calculate a projected vorticity advection Π^{A_ω} by computing the eigenvectors and eigenvalues of the vorticity gradient.

Experimental validation of the numerical model

The validation of the direct numerical simulation results in the stenosed aorta case from the comparison with *in vitro* time-resolved three-dimensional flow magnetic resonance imaging can be found in Corso *et al.*[10]. With respect to the experimental validation of the fluid-structure interaction computational model of the bioprosthetic aortic valve case from *in vitro* experiments, Figure 8 shows the very good agreement both qualitatively and quantitatively between the numerical FSI results and *in vitro* measurements[2,16]. The leaflet kinematics during valve opening for the VLth30 BioAV (see Fig. 6 (c)) is in very good agreement with the images recorded at three time instants with a high-speed camera and presented in[2] (cf. Fig. 8 (b)). Furthermore, the comparison of the area at the vena contracta between the numerically and experimentally evaluated values over systole is presented in Fig. 8 (c). We notice a good agreement of the VLth30 curve obtained from the numerical flow velocity data with the diamond-shaped markers representing the area calculated based on the phase-averaged velocity field obtained from tomographic particle image velocimetry (tomo-PIV) measurements[16]. From the graph at Fig. 8 (c), we also observe that, for the VLth30 BioAV case, the area where the flow velocity is the highest periodically varies in time at variable frequencies between 18 and 30 Hz[11]. Conversely, the BioAV with Ulth0 design does not exhibit periodic motion of the three leaflets during peak systole (refer to Fig. S1 (a, c) in the supporting information), unlike the VLth30 case where the three leaflets move periodically at distinct frequencies[11] and asymmetrically relative to the centerline of the aortic root (see

Fig. S1 (b, d) in the supporting information). A more in-depth analysis of the correlation between the kinetic energy carried by the leaflets and the kinetic energy calculated in the flow over spherical regions is presented in the second part of this study[12]. The flow characteristics highlighted by the streamlines of the time-averaged velocity field obtained from the 3D FSI simulation are in line with those observed in experimental tomo-PIV data. The tomo-PIV data were acquired using a silicone phantom model of the ascending aorta with the *Edwards Intuity Elite* BioAV (Edwards Lifesciences, Irvine, CA, United States) positioned in the sinus of Valsalva portion of the aorta model[16]. For comparison, the experimental velocity field was phase-averaged over peak systole. Notably, a high-velocity jet is present in the middle of the aorta, as indicated by streamlines aligned with the aorta's centreline. Additionally, recirculation zones are observed and align with the three posts of the BioAV ring. The curves in Fig. 8 (f) showing slice-averaged turbulence intensity, which represent the magnitude of velocity fluctuations owing to turbulence relative to the strength of the mean flow velocity, are nearly coincident for various slices perpendicular to the centerline of the ascending aorta. This observation underscores the remarkable consistency between the *in vitro* experiment utilising the silicone phantom model and the numerical simulations including the VLth30 BioAV model.

[Figure 8 about here.]

Acknowledgements

This work was supported by the computational resources from the Swiss National Supercomputing Centre (CSCS) under project IDs c12, s1012 and sm56.

P. Corso would like to thank F. B. Coulter (ETH Zürich) for providing the computer-aided sketch of the sheet-like leaflet geometry. This sketch was instrumental in generating the final three-dimensional and volumetric geometrical model of the VLth30 BioAV for the present study. P. Corso also acknowledges the support of M. G. C. Nestola from Università della

Svizzera italiana (USI) on the solid solver and on the part of the code dealing with the coupling of the two solvers.

Author contribution

P. Corso: Conceptualisation, Data curation, Formal analysis, Interpretation of the results, Investigation, Methodology, Software, Visualisation, Writing - original draft. **D. Obrist:** Funding acquisition, Input on the results and on the original draft.

Declaration of competing interest

The authors declare that they have no known competing financial interests or personal relationships that could have appeared to influence the work reported in this paper.

References

1. Auricchio F., Conti M., Ferrara A., Morganti S. and Reali A., *Patient-specific simulation of a stentless aortic valve implant: the impact of fibres on leaflet performance*, Computer methods in biomechanics and biomedical engineering, 17(3):277-285, 2014.

2. Bailoor S., Seo J.-H., Dasi L.,*et al. A computational study of the hemodynamics of bioprosthetic aortic valves with reduced leaflet motion*, J. Biomech., 120, 2021.

3. Becsek B., Pietrasanta L. and Obrist D., *Turbulent Systolic Flow Downstream of a Bioprosthetic Aortic Valve: Velocity Spectra, Wall Shear Stresses, and Turbulent Dissipation Rates*, Front. in physiol. 11:539-575, 2020.

4. Bodony D. J., *Analysis of sponge zones for computational fluid mechanics*, J. Comput. Phys., 212, 681-702, 2006.

5. Caballero A.D., Laín S.J.C.E., *A review on computational fluid dynamics modelling in human thoracic aorta*, Cardiovasc. Engng Technol., 4(2):103–130, 2013.

6. Canuto C., Hussaini M. Y., Quarteroni A., Zang T. A., *Spectral Methods: Evolution to Complex Geometries and Applications to Fluid Dynamics*, Spinger, 2007.

7. Chen Y., Luo H., *A computational study of the three-dimensional fluid-structure interaction of aortic valve*, J. Fluids and Structures., 80:332-349, 2018.

8. Corso P., Gülan U., Cohrs N., *et al.*, *Comprehensive In Vitro Study of the Flow Past Two Transcatheter Aortic Valves: Comparison with a Severe Stenotic Case*, Ann. Biomed. Eng., 47(11):2241-2257, 2019.

9. Corso P., Giannakopoulos G., Gulan U., *et al.*, *A Novel Estimation Approach of Pressure Gradient and Haemodynamic Stresses as Indicators of Pathological Aortic Flow Using Subvoxel Modelling*, IEEE Trans. Biomed. Eng., 68(3):980-991, 2021.

10. Corso P., Walheim J., Dillinger H., *et al.*, *Toward an accurate estimation of wall shear stress from 4D flow magnetic resonance downstream of a severe stenosis*, Magn. Res. Med. 86(3):1531-1543, 2021.

11. Corso P., Coulter F. B., Nestola M. G. Ch., *et al.*,*Study Of The Flutter Kinematics And Blood Flow Motion For Bioprosthetic Aortic Valves With Different Designs*, Heart Valve Society's Annual Meeting, March 2022.

12. Corso P., Obrist D., *On the role of aortic valve architecture for physiological haemodynamics and valve replacement. Part II: spectral analysis and anisotropy*, 2023.

13. Deville M. O., Fischer P. F, Mund E. H. *High-Order methods for incompressible fluid flow*. Cambridge Monographs on Applied and Computational Mathematics. Cambridge University Press; 2002.

14. Friedlander S., Lipton-Lifschitz A., *Chapter 8 - Localized Instabilities in Fluids*, Handbook of Mathematical Fluid Dynamics, 2:289-354, 2003.

15. Frost W., Moulden T. H., *Handbook of Turbulence: volume 1 - Fundamentals and Applications*, Plenum Press, 1977

16. Hasler D., Obrist D, *Three-dimensional flow structures past a bio-prosthetic valve in an in-vitro model of the aortic root*, PLOS One, 13(3), 2018.

17. Henniger R., Obrist D., Kleiser L., *High-order accurate solution of the incompressible Navier–Stokes equations on massively parallel computers*. J. of Comp. Phys, 229(10):3543-3572, 2010.

18. Holzapfel G. A., Gasser Th. C., Ogden R. W., *A New Constitutive Framework for Arterial Wall Mechanics and a Comparative Study of Material Models*, Journal of elasticity and the physical science of solids, 61(1):1-48, 2000.

19. Hussain A. K. M. F., Reynolds W. C., *The mechanics of an organized wave in turbulent shear flow*. J. Fluid Mech., 41(2):241-258, 1970.

20. Jeong J., Hussain F., *On the identification of a vortex*, J. Fluid Mech., 285:69-94, 1995.

21. Johnson E. L., Wua M. C. H., Xu F. *et al.*, *Thinner biological tissues induce leaflet flutter in aortic heart valve replacements*. Proc. Nat. Acad. Sciences, 117(32):19007-19016, 2020.

22. Krause R., Zulian P., *A Parallel Approach to the Variational Transfer of Discrete Fields between Arbitrarily Distributed Unstructured Finite Element Meshes*, SIAM J. on Scientific Comp., 2016.

23. Marom G., Peleg M., Halevi R., *et al.*, *Fluid-structure interaction model of aortic valve with porcine-specific collagen fiber alignment in the cusps*, J. Biomech. Eng., 135(10), 2013.

24. Mattor N., Williams T. J., Hewett D. W., *Algorithm for solving tridiagonal matrix problems in parallel*, Parallel Comput., 21:1769–1782, 1995.

25. Morany A., Lavon K., Bardon R. G., Kovarovic B., Hamdan A., Bluestein D., Haj-Ali R., *Fluid-structure interaction modeling of compliant aortic valves using the lattice Boltzmann CFD and FEM methods*, Biomechanics and Modeling in Mechanobiology, 22:837-850, 2023.

26. NEK5000 v19.0. Argonne National Laboratory, Illinois, 2020. [Online]. Available: https://nek5000.mcs.anl.gov

27. Nestola M. G. Ch., Becsek B., Zolfaghari H., *et al.*, *An immersed boundary method for fluid-structure interaction based on variational transfer*, J. Comp. Phys. 398, 2019.

28. Nguyen V., Michel M., Eltchaninoff H., *et al.*, *Implementation of Transcatheter Aortic Valve Replacement in France*, J. Am. College Card., 71(15), 2018.

29. Kitware and Inc. *VTK User's Guide* Kitware Inc., 11$^{\text{th}}$ edition, 3 2010. ISBN 978-1930934238.

30. Permann C. J., Gaston D. R., Andrs D., Carlsen R. W., Kong F., Lindsay A. D., *et al.*, *MOOSE: Enabling massively parallel multiphysics simulation*, SoftwareX. 11, 2020.

31. Peskin Ch. S., *The immersed boundary method*. Acta Numerica, 479-517. Cambridge University Press, 2002.

32. Petitjeans P., *Stretching of a vortical structure: filaments of vorticity*, Europhysics News, 34(1):20-23, 2003.

33. Balay S., Abhyankar S., Adams MF, Benson S, Brown J, Brune P, Buschelman K., Constantinescu E. M., Dalcin L, Dener A., Eijkhout V., Faibussowitsch J., Gropp W. D., Hapla V., Isaac T., Jolivet P., Karpeev D., Kaushik D., Knepley M. G., Kong F., Kruger S., May D. A., Curfman McInnes L., Tran Mills T., Mitchell L., Munson T., Roman J. E., Rupp K., Sanan P., Sarich J., Smith B. F., Zampini S., Zhang H., Zhang J., *PETSc Web page*, https://petsc.org/, 2023.

34. Pujari SH, Agasthi P. Aortic Stenosis. [Updated 2022 Apr 14]. In: StatPearls [Internet]. Treasure Island (FL): StatPearls Publishing; 2022 Jan-. Available from: https://www.ncbi.nlm.nih.gov/books/NBK557628/

35. Tsolaki E., Corso P., Zboray R., Avaro J. *et al.*, *Multiscale Multimodal Characterization and Simulation of Structural Alterations in Failed Bioprosthetic Heart Valves*. Acta Biomaterialia, 169(10):138-154, 2023.

36. Vogl B., Gadhave R., Wang Z., *et al.*, *Effect of aortic curvature on bioprosthetic aortic valve performance*, J. Biomech., 146(1), 2023.

37. Williams M. H., *Vorticity amplification and annihilation in a potential vortex*, Phys. Fluids 4:1467–1471, 1992.

38. Yoganathan A. J., He S., Jones S. C. *Fluid mechanics of heart valves.* Annu. Rev. Biomed. Eng., 6:331–362, 2004.

List of Figures

1 Jet geometries (highlighted by velocity magnitude) for the three valvular cases at 8 time instances. The plane of investigation is positioned at a distance of 10 mm from the sino-tubular junction (STJ). The eccentricity from the centre of the circular cross-section is quantified by the distance ε_c and the azimuthal angle α_c in the plane. The centre of the cross-section is displayed by a black dot while the centre of mass of the jet region is represented by a white dot. 29

2 Velocity magnitude for the three valvular cases at 8 time instances in a plane located at a distance of 24 mm from the STJ. 30

3 Coherent vortical structures downstream of the considered severe aortic stenosis and of the two newly designed bioprosthetic aortic valves. The vortical structures are highlighted using a negative value for the λ_2 criterion proposed by Jeong and Hussain[20]. Velocity magnitude in two transverse planes (normal to the centreline) is also displayed. The time between two consecutive images is equal to 0.03 s. 31

4 Quantities based on the terms of the vorticity dynamics equation for the three valvular cases. (a) Time evolution of the spatially averaged vortex stretching magnitude. (b) Time series of the projected vortex stretching averaged over the VoI. (c) Relative intensity of the projected advection and vorticity over time (d) Table with the spatially and temporally averaged quantities of the vorticity transport equation. 32

5 Geometrical description of ascending aorta models (a, b, c) including an aortic stenosis model due to calcified leaflets (b, e, f) as well as two bioprosthetic aortic valves inserted (d) in a realistic aortic root geometry (c, d, g, h). . . . 33

6 Geometrical description of the two different geometries of valve bioprostheses (a, b, c) obtained by modifying the leaflet shape (d, e), the valve ring being the same for both valves (a). The parameters describing the three features, i.e. the belly curve, the free edge and the shape of the attachment curve, for the leaflet geometry generation, are summarised in (f). 34

7 Evolution of the inflow rate and Reynolds number in the numerical model of the aortic valve stenosis and of the aortic valve bioprostheses. 35

8 Experimental validation of the FSI numerical model under peak systolic conditions. Leaflet opening (a) simulated for the VLth30 bioprosthetic valve case and (b) recorded by a high-speed camera during *in vitro* experiments[2] (c) Area at the vena contracta downstream of the two simulated BioAV cases obtained from the FSI numerical simulations and downstream of the *Edwards Intuity Elite* BioAV extracted from the flow field measured using the tomographic particle image velocimetry technique[16]. (d) Streamlines along the velocity field averaged over systole downstream of the VLth30 valve model. (e) Streamlines along the phase-averaged velocity obtained from tomo-PIV measurements. (f) Non-dimensional slice-averaged turbulence intensity from the simulation (VLth30 BioAV case) and from tomo-PIV experiments. 36

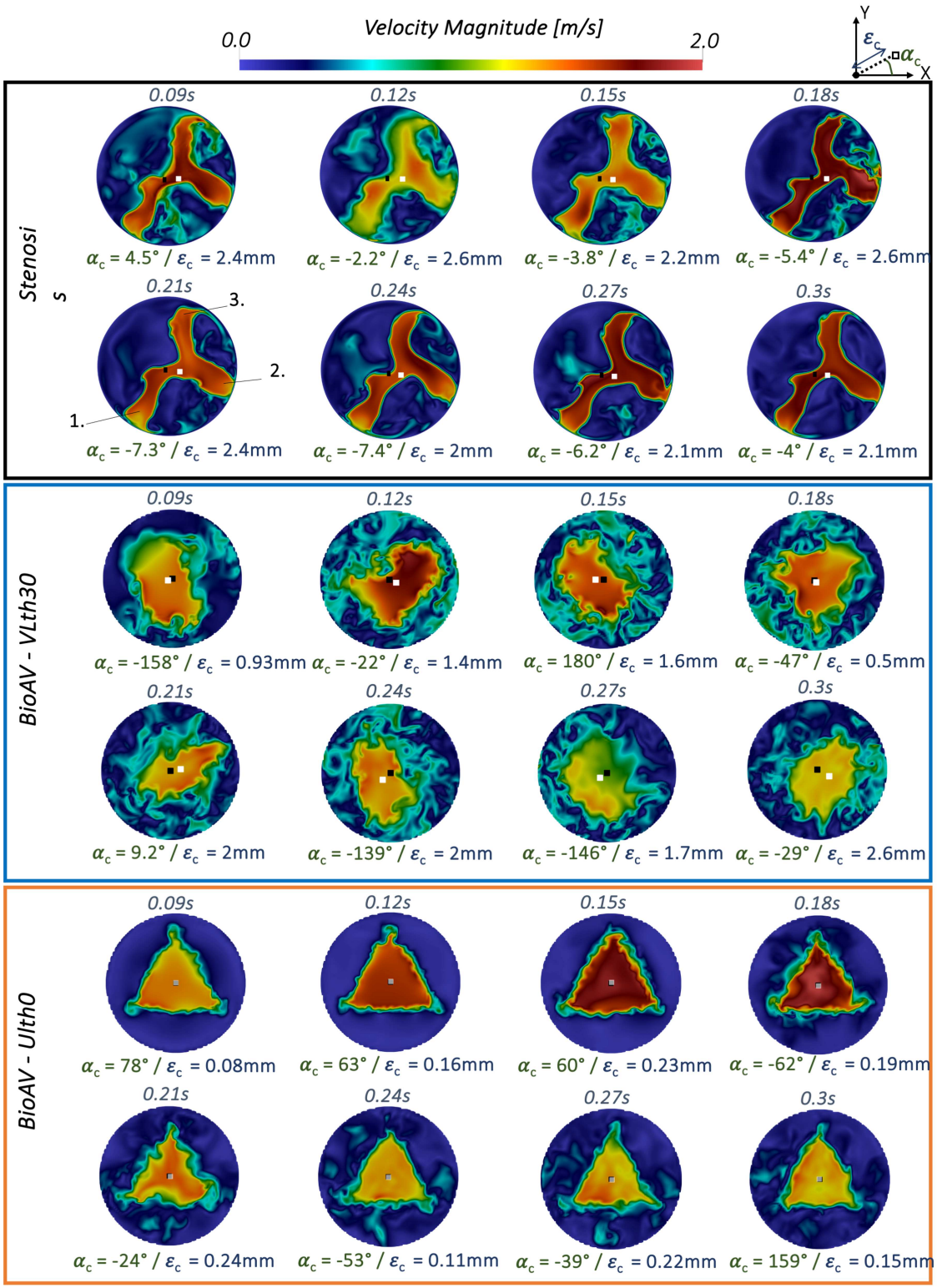

Figure 1: Jet geometries (highlighted by velocity magnitude) for the three valvular cases at 8 time instances. The plane of investigation is positioned at a distance of 10 mm from the sino-tubular junction (STJ). The eccentricity from the centre of the circular cross-section is quantified by the distance ε_c and the azimuthal angle α_c in the plane. The centre of the cross-section is displayed by a black dot while the centre of mass of the jet region is represented by a white dot.

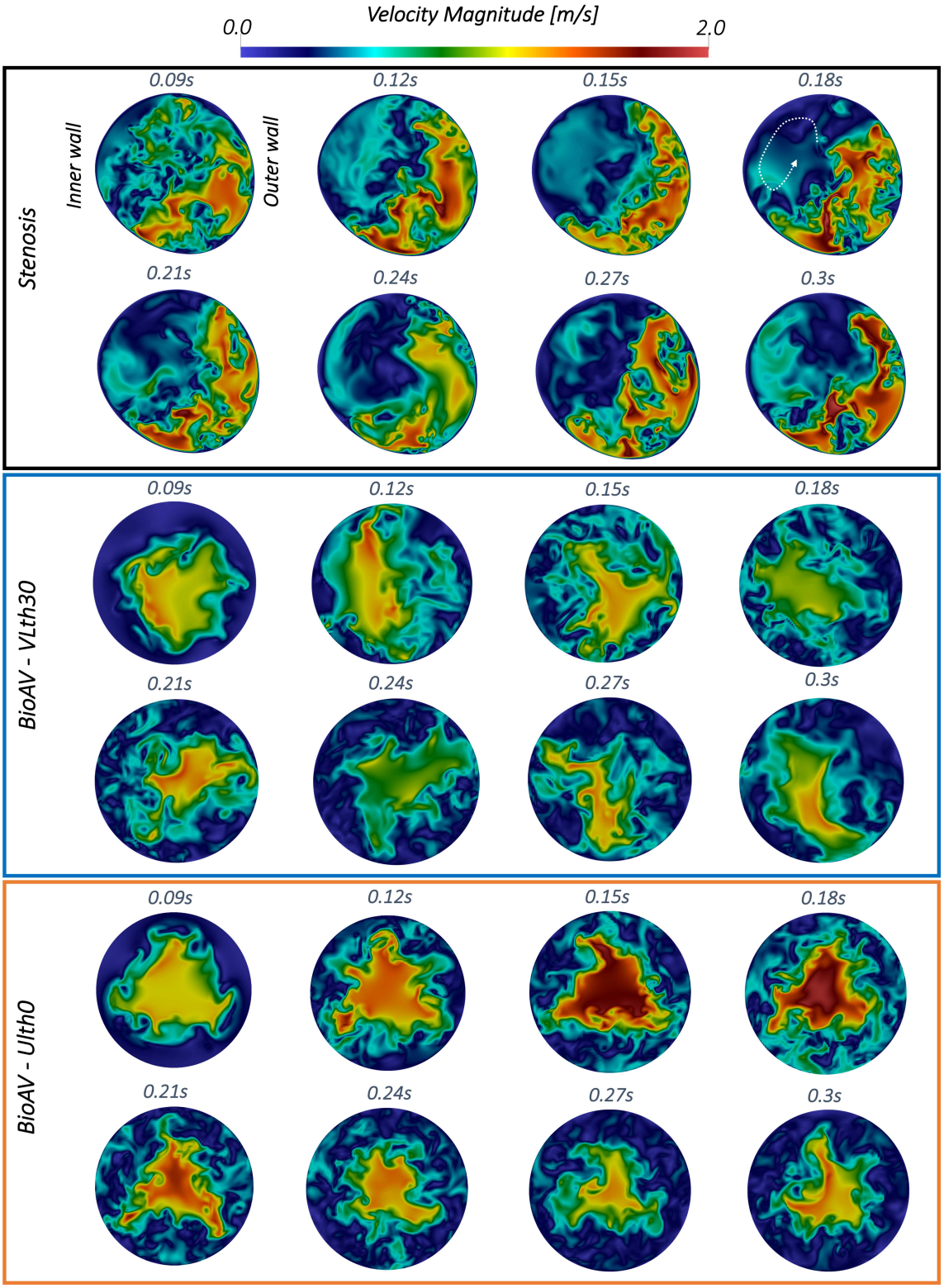

Figure 2: Velocity magnitude for the three valvular cases at 8 time instances in a plane located at a distance of 24 mm from the STJ.

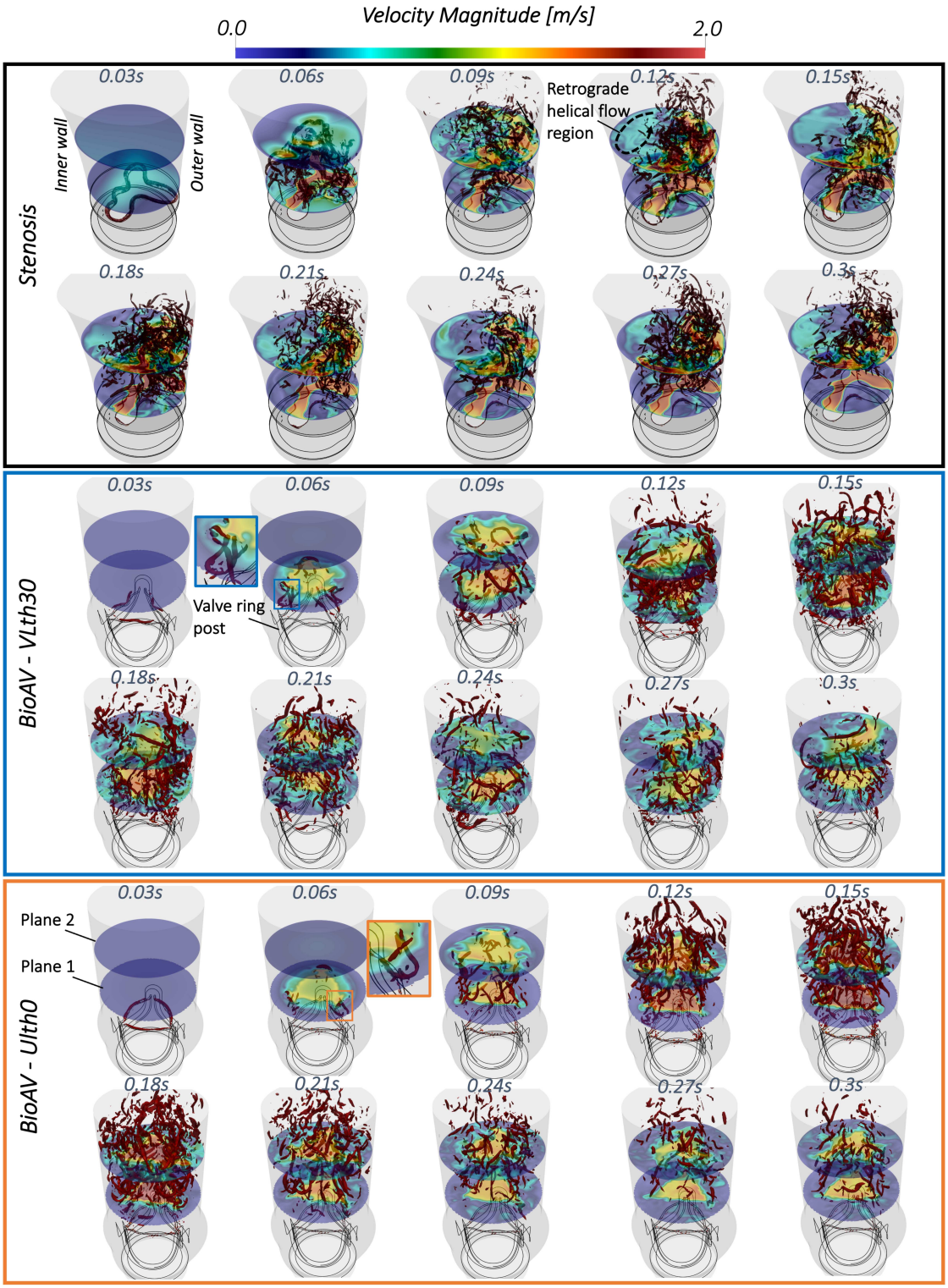

Figure 3: Coherent vortical structures downstream of the considered severe aortic stenosis and of the two newly designed bioprosthetic aortic valves. The vortical structures are highlighted using a negative value for the λ_2 criterion proposed by Jeong and Hussain[20]. Velocity magnitude in two transverse planes (normal to the centreline) is also displayed. The time between two consecutive images is equal to 0.03 s.

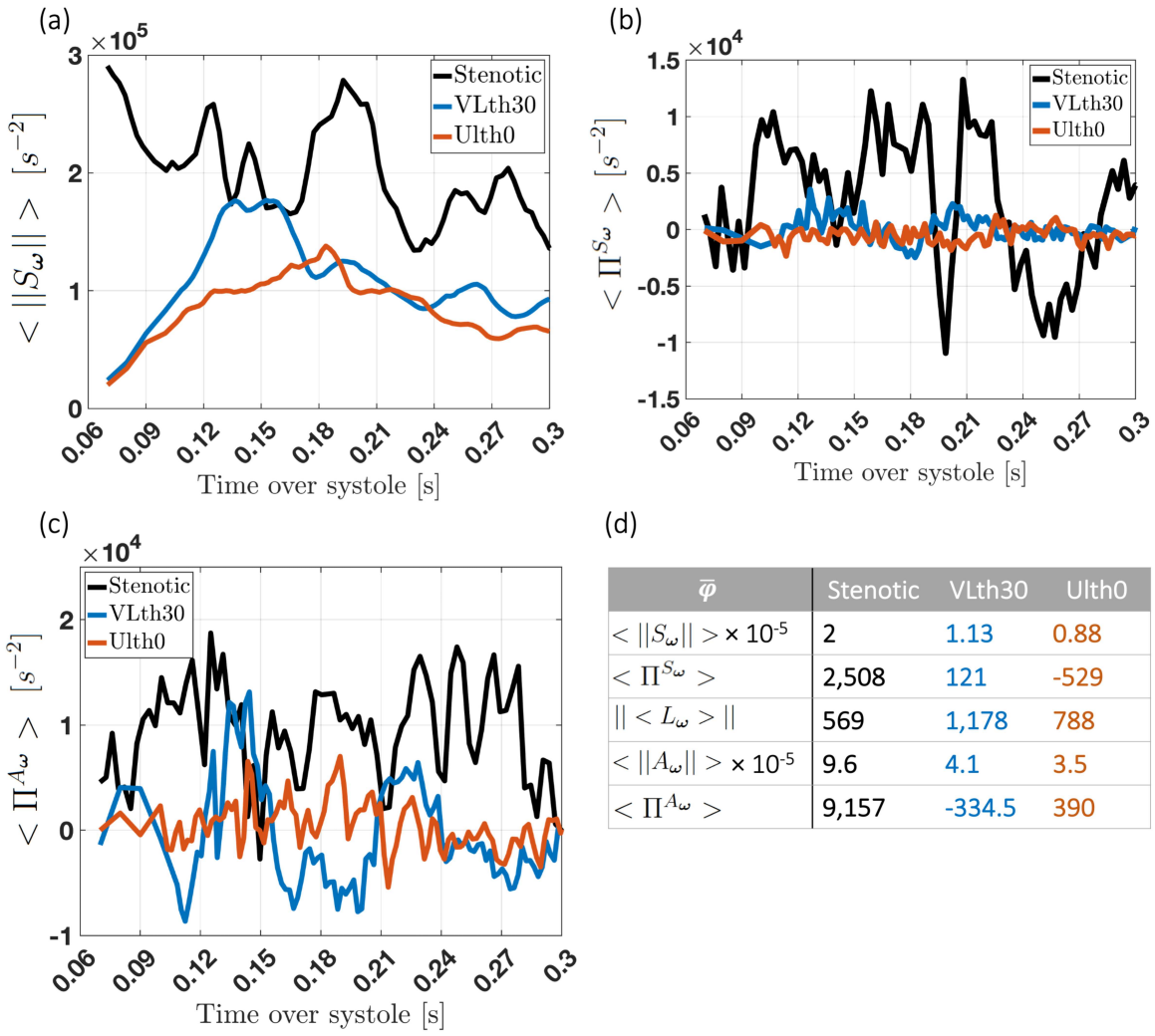

$\bar{\varphi}$	Stenotic	VLth30	Ulth0
$< \|\|S_\omega\|\| > \times 10^{-5}$	2	1.13	0.88
$< \Pi^{S_\omega} >$	2,508	121	-529
$\|\| < L_\omega > \|\|$	569	1,178	788
$< \|\|A_\omega\|\| > \times 10^{-5}$	9.6	4.1	3.5
$< \Pi^{A_\omega} >$	9,157	-334.5	390

Figure 4: Quantities based on the terms of the vorticity dynamics equation for the three valvular cases. (a) Time evolution of the spatially averaged vortex stretching magnitude. (b) Time series of the projected vortex stretching averaged over the VoI. (c) Relative intensity of the projected advection and vorticity over time (d) Table with the spatially and temporally averaged quantities of the vorticity transport equation.

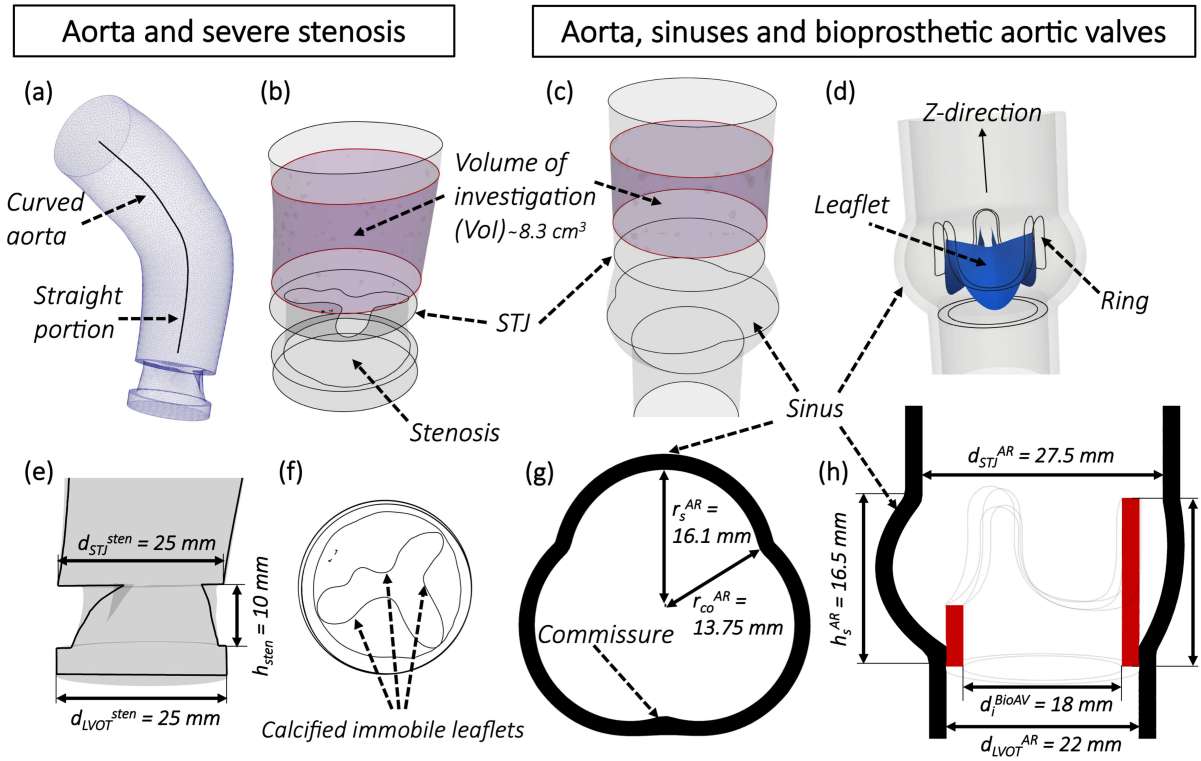

Figure 5: Geometrical description of ascending aorta models (a, b, c) including an aortic stenosis model due to calcified leaflets (b, e, f) as well as two bioprosthetic aortic valves inserted (d) in a realistic aortic root geometry (c, d, g, h).

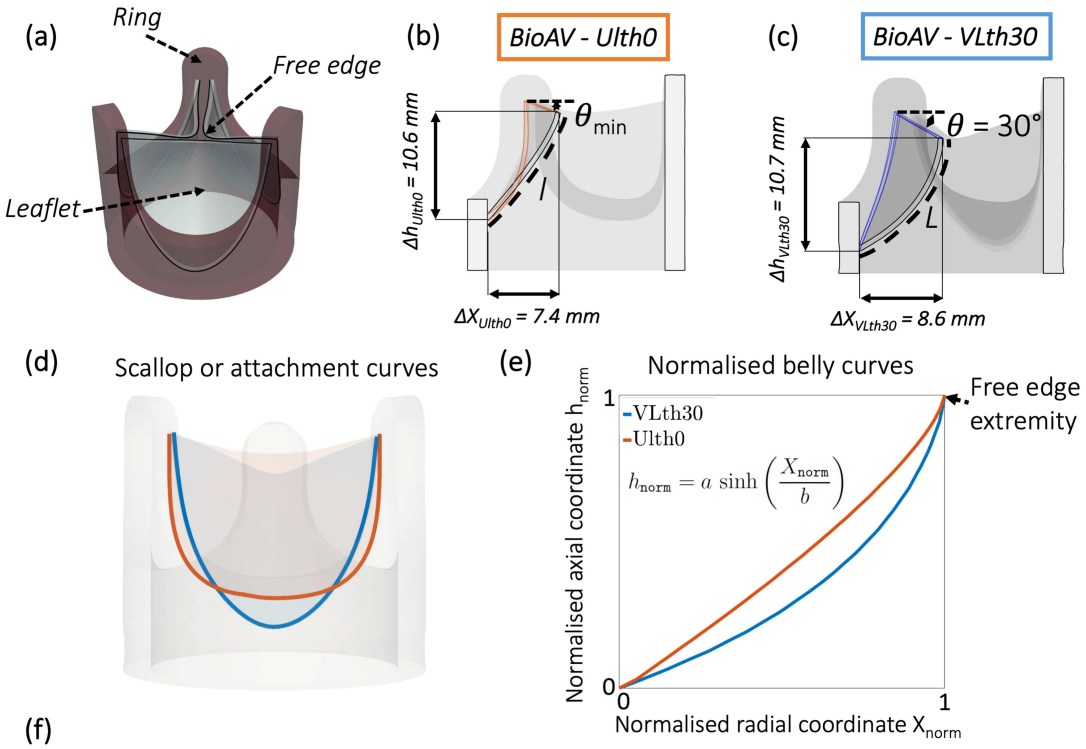

Nomenclature	Scallop curve	Belly curve	Free edge angle
VLth30	V-shaped	Belly length L= 14.5 mm a = 0.44 b = 1.17	θ = 30°
Ulth0	U-shaped	Belly length l = 13 mm a = 1.61 b = 2.23	θ = 0°

Figure 6: Geometrical description of the two different geometries of valve bioprostheses (a, b, c) obtained by modifying the leaflet shape (d, e), the valve ring being the same for both valves (a). The parameters describing the three features, i.e. the belly curve, the free edge and the shape of the attachment curve, for the leaflet geometry generation, are summarised in (f).

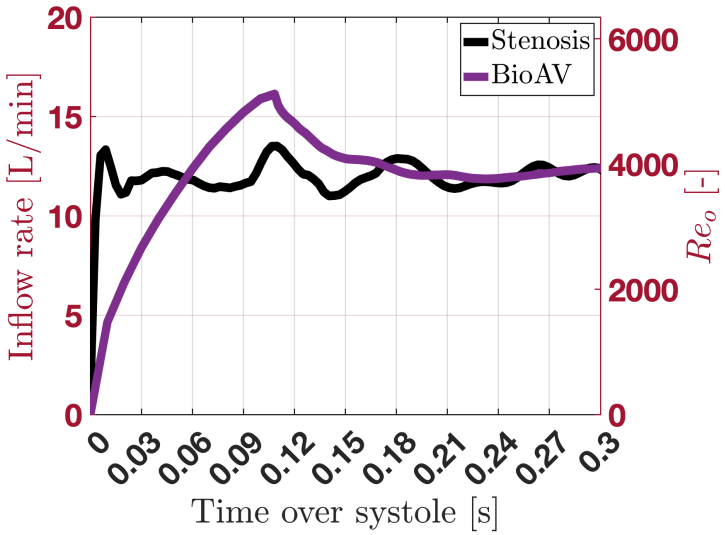

Figure 7: Evolution of the inflow rate and Reynolds number in the numerical model of the aortic valve stenosis and of the aortic valve bioprostheses.

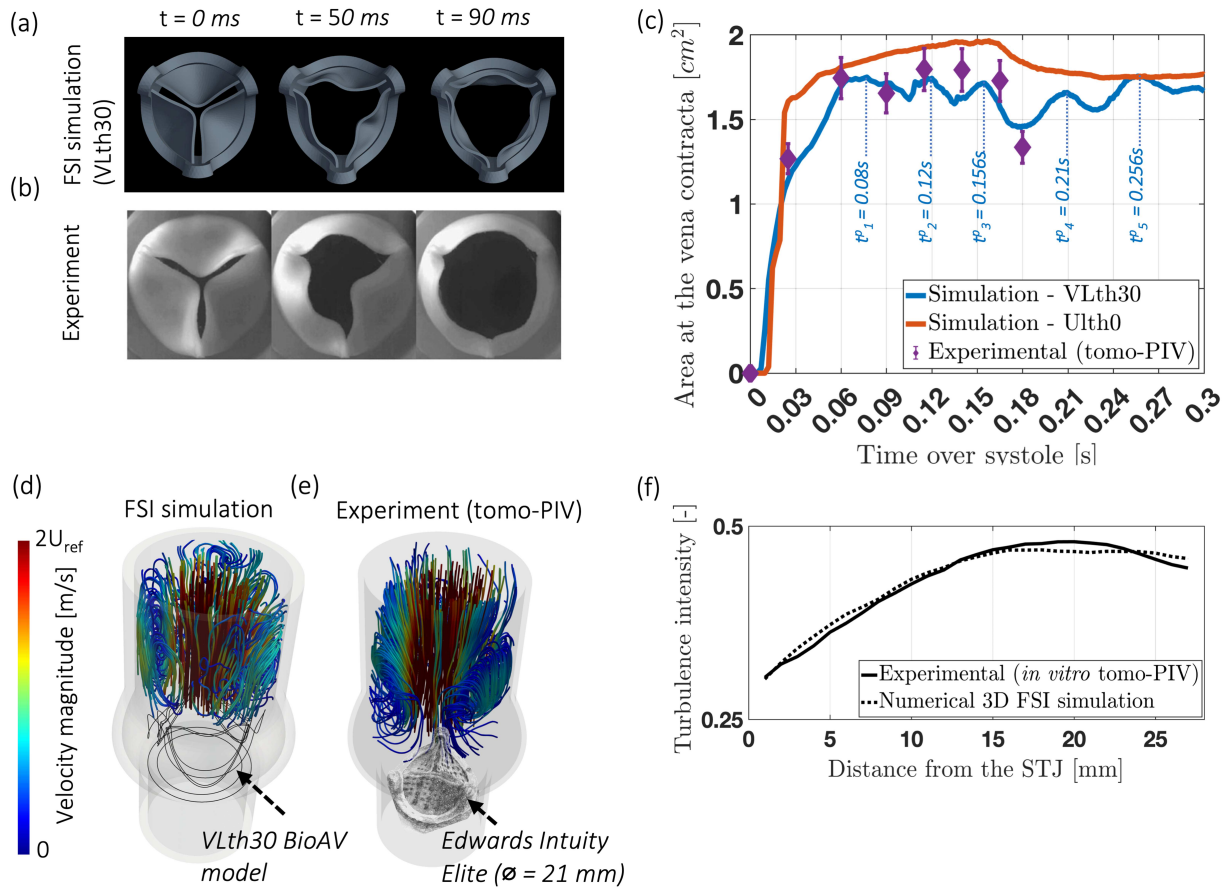

Figure 8: Experimental validation of the FSI numerical model under peak systolic conditions. Leaflet opening (a) simulated for the VLth30 bioprosthetic valve case and (b) recorded by a high-speed camera during *in vitro* experiments[2] (c) Area at the vena contracta downstream of the two simulated BioAV cases obtained from the FSI numerical simulations and downstream of the *Edwards Intuity Elite* BioAV extracted from the flow field measured using the tomographic particle image velocimetry technique[16]. (d) Streamlines along the velocity field averaged over systole downstream of the VLth30 valve model. (e) Streamlines along the phase-averaged velocity obtained from tomo-PIV measurements. (f) Non-dimensional slice-averaged turbulence intensity from the simulation (VLth30 BioAV case) and from tomo-PIV experiments.

List of Tables

1 Table of the non-dimensional quantities based on the terms of the momentum conservation along the streamwise direction for the three valvular cases presented in this work and for the cases presented in Chen and Luo[7] and Becsek *et al.*[3]. 38

Table 1: Table of the non-dimensional quantities based on the terms of the momentum conservation along the streamwise direction for the three valvular cases presented in this work and for the cases presented in Chen and Luo[7] and Becsek *et al.*[3].

	$\overline{\Delta P\, A}$	$\overline{\bar{p}}$	$\overline{C_D}$	$\max C_D$	$\overline{h_{F_{\text{leaflets}}}}/\varnothing$
1. Stenotic - Corso et al.[9]	0.746	0.037	1.42	3.36 at t=0.083 s	2
2. BioAV - VLth30	0.432	0.14	0.175	0.24 at t=0.108 s	0.5
3. BioAV - Ulth0	0.459	0.072	0.103	0.14 at t=0.154 s	0.33
4. BioAV - similar case as that presented in Becsek et al.[3]	0.387	0.081	0.502	0.94 at t=0.122 s	1.12
5. Flexible AV - Chen and Luo[7]	0.477	0.16	0.47	1.04 at t=0.18 s	2.23

Supplementary Files

This is a list of supplementary files associated with this preprint. Click to download.

- ManuscriptvalveDesignPart1PasSINatBiomed.pdf